Uzbek Journal "Problems of Mechanics"

Research Article

DOI: 10.68846/pmjournal-2026-37-00008

A two-scale numerical model of mass transport and adsorption in a cylindrical radial-flow filter

Bakhtiyor I.Boborahimov[1*], **Mohinur U.Ermonova**[2], **Lochinbek S.Usmonov**[2]

[1] Digital Technologies and Artificial Intelligence Development Research Institute, 17A Buz-2, Tashkent, 100125, Uzbekistan
[2] Gulistan State Pedagogical Institute, 48 Istiqlol Street, Gulistan, 120105, Uzbekistan
[3] Zarmed University, Samarkand, 140129, Uzbekistan
[*] **Corresponding author:** uzbekpy@gmail.com

Received: 28 June 2026 | **Revised:** 15 August 2026 | **Accepted:** 05 September 2026 | **Published:** 30 September 2026

ABSTRACT

A two-scale (macro–micro) mathematical model and a verified numerical method are developed for mass transport and adsorption in an annular cylindrical filter under inward radial flow. At the macro scale, an axisymmetric advection–dispersion equation with the interstitial velocity $|u_r| \propto 1/r$ is coupled, through external film transfer and local Langmuir equilibrium, to intraparticle surface diffusion inside spherical granules resolved by the homogeneous surface diffusion model. The film coefficient and the radial dispersion are made velocity-dependent through standard Sherwood and dispersivity correlations. The complete dimensionless problem is derived and the governing groups (radial Peclet number, capacity ratio, Biot number, granule diffusion time, and a radius-dependent Damköhler number) are evaluated for a representative granular-activated-carbon case; for these parameters the process is intraparticle-diffusion limited, with $Da_p \sim 10^2$–10^3. The model is reduced to the classical linear-driving-force law in the fast-diffusion, negligible-film limit. The numerical method combines a conservative finite-volume discretisation on an equal-volume radial grid, Strang operator splitting, and a spectral (modal) reduction of the granule problem. Grid, time-step, and modal convergence, machine-precision global mass conservation, solution positivity, and agreement with the linear-driving-force limit are demonstrated. A controlled comparison against a uniform-velocity bed of equal residence time shows that, at constant intraparticle diffusivity, the radial velocity field mainly redistributes the internal loading while leaving the outlet breakthrough close to the uniform-velocity case.

KEYWORDS

radial-flow adsorber, two-scale model, homogeneous surface diffusion, film mass transfer, finite-volume method, spectral reduction, breakthrough curve.

1. Introduction

Adsorption on granular activated carbon (GAC) and related porous sorbents is one of the most widespread methods for removing heavy-metal ions, organic micropollutants, pesticides, and pharmaceutical residues from water, owing to its efficiency, simple operation, and low cost [1]. The thermodynamic and kinetic foundations of adsorption, including isotherm and kinetic models, are treated in the classical monographs [2]. Equilibrium is most often described by the Langmuir isotherm, which assumes a finite number of energetically identical sites, each binding one molecule [3]. In fixed-bed dynamics, the principal engineering output is the breakthrough curve, which fixes the service life of the filter; its analytical and numerical modelling, and the limits of the simplifying assumptions commonly used, have been reviewed in detail [4–6].

The rate-limiting step in liquid-phase adsorption is usually intraparticle transport. The lumped linear-driving-force (LDF) equation condenses this mechanism into a single coefficient that is not a material property but an adjustable quantity depending on velocity, granule size, and concentration, and is therefore not predictive across operating regimes. The homogeneous surface diffusion model (HSDM) instead resolves intraparticle diffusion explicitly and has been used to predict breakthrough in full-scale GAC filters [7]; its numerical and semi-analytical solutions [8], its extension to different granule geometries [9], and the experimental determination of the governing surface diffusivities [10] are well established. The HSDM reduces to LDF through the Glueckauf approximation in the fast-diffusion limit, with $k_{LDF} = 15D_s/R_p^2$ [11]. The mathematical theory of diffusion in a sphere, including the eigenfunction expansions used below for the spectral reduction, is given in the classical reference [12].

Macroscopic liquid-phase transport combines advection and hydrodynamic dispersion [13, 14]; external film transfer is customarily obtained from a Sherwood correlation [15], and mechanical dispersion from a velocity-proportional dispersivity [14]. Analytical solutions of advection–dispersion equations with distance-dependent coefficients [16] indicate the mathematical difficulty introduced by a spatially varying velocity, which is exactly the situation in radial geometry, where $|u_r| \propto 1/r$.

Radial-flow adsorbers, in which the fluid crosses a cylindrical bed in the radial direction, have been studied mainly for gas-phase processes — air drying, oxygen production, catalytic conversion — where the nonuniform velocity is usually regarded as a design defect to be removed by flow distributors [17–19]. Within the regional research school, filtration and transport in cylindrical porous filters have been modelled by the finite-volume method [20], and the upscaling of adsorbing-solute transport from pore to macro scale has been analysed by pore-network modelling [21], supporting the two-scale description used here.

This survey shows that two-scale models resolving intraparticle diffusion are well developed for axial, uniform-velocity beds, whereas liquid-phase radial geometry with $|u_r| \propto 1/r$ has received little attention. The present work addresses this gap not by claiming a large new physical effect, but by providing a carefully verified modelling and numerical framework and by quantifying, honestly, how much the radial velocity field actually matters. The contributions are: (i) a two-scale radial model that couples variable-velocity advection–dispersion, with

velocity-dependent film and dispersion coefficients, to resolved intraparticle surface diffusion; (ii) the complete dimensionless formulation, with corrected governing groups and a radius-dependent Damköhler number obtained from a consistent residence-time analysis; (iii) a conservative finite-volume/spectral-reduction algorithm whose grid, time, and modal convergence, mass conservation, positivity, and LDF-limit consistency are demonstrated within the paper; and (iv) a controlled comparison against a uniform-velocity bed that isolates the influence of the $1/r$ velocity field. The full nomenclature is collected at the end of the paper.

2. Problem statement

The system is described at two spatial scales. The *macro* scale is the annular adsorbent bed between the outer radius R_{out} and the inner (core) radius R_{in}; water enters through the outer lateral surface, flows radially inward toward the perforated core, and the contaminant is carried by advection and spread by dispersion. The *micro* scale is each spherical granule (radius R_p): solute crosses the external liquid film, then diffuses inward as an adsorbed species by surface diffusion, with local Langmuir equilibrium at the granule surface. The model is one-dimensional in the macro radial coordinate r: axial symmetry ($\partial/\partial\theta \equiv 0$) and axial homogeneity ($\partial/\partial z \equiv 0$) are assumed. This restricts the model to configurations in which inlet distribution, end effects, and packing nonuniformity along z are negligible; the applicability and limitations of this assumption are discussed in Section 5.

The following closure assumptions are adopted: (a) spherical, monodisperse granules; (b) isothermal, dilute conditions, so that porosity and physical properties are concentration-independent; (c) a constant intraparticle surface diffusivity D_s (a material property of the granule); (d) local Langmuir equilibrium at the granule surface; (e) an incompressible, prescribed radial flow field.

Flow field. The velocity is not obtained from a pressure (Darcy) solution; it is fixed kinematically by mass conservation. Since the constant volumetric flow rate Q must cross every cylindrical surface of radius r and height L, the *superficial* (Darcy) and *interstitial* (pore) velocities are, respectively,

$$\begin{aligned} q_r(r) &= -\frac{Q}{2\pi r L}, \\ u_r(r) &= \frac{q_r(r)}{\varepsilon} = -\frac{Q}{2\pi r L \varepsilon}, \\ |u_r| &\propto \frac{1}{r}, \end{aligned} \tag{1}$$

with ε the bed porosity and the negative sign denoting inward flow. This field satisfies $\nabla \cdot \mathbf{q} = \frac{1}{r}\partial_r\,(r q_r) = 0$ identically. The transport equation below is written with the interstitial velocity u_r, which is the velocity that advects the dissolved solute through the pore space; this distinction (superficial vs. interstitial) is kept throughout.

Macroscopic balance. A solute balance over a bulk ring element, per unit pore volume, gives the axisymmetric advection–dispersion–sorption equation

$$\begin{aligned} &\frac{\partial C}{\partial t} + \frac{\rho_b}{\varepsilon}\frac{\partial \overline{q}}{\partial t} \\ &= \frac{1}{r}\frac{\partial}{\partial r}\left(r\, D_r(r)\frac{\partial C}{\partial r}\right) - u_r(r)\frac{\partial C}{\partial r}, \end{aligned} \tag{2}$$

where C is the liquid concentration (per unit liquid volume), $\overline{q}$ the granule-averaged solid loading, $\rho_b = (1-\varepsilon)\rho_p$ the bed bulk density, and ρ_p the granule density. The factor ρ_b/ε converts the solid uptake rate (per unit solid mass) into a liquid-phase sink (per unit pore volume). The uptake term $\frac{\rho_b}{\varepsilon}\partial_t \overline{q}$ is *not* an empirical LDF term: $\overline{q}$ is delivered by the resolved granule problem below.

Velocity-dependent coefficients. Because the same $1/r$ field that constitutes the geometric feature of the problem also changes the local hydrodynamics, the film and dispersion coefficients are made velocity-dependent rather than constant. The film coefficient follows the Wakao–Funazkri correlation [15]

$$\begin{aligned} Sh(r) &= 2 + 1.1\, Sc^{1/3}\, Re_p(r)^{0.6}, \\ Re_p(r) &= \frac{d_p\ |u_r(r)|}{\nu}, \\ Sc &= \frac{\nu}{D_m}, \\ k_f(r) &= \frac{Sh(r)\, D_m}{d_p}, \end{aligned} \tag{3}$$

with $d_p = 2R_p$, ν the kinematic viscosity, and D_m the molecular diffusivity; the radial dispersion is

$$D_r(r) = \frac{D_m}{\sqrt{2}} + \alpha_L\ |u_r(r)|\,, \tag{4}$$

with α_L the longitudinal dispersivity. Equations (3)–(4) make k_f and D_r larger near the core, where the velocity is higher.

Granule (micro) problem. Inside each granule the loading obeys spherical surface diffusion, and the average loading is a volume integral,

$$\begin{aligned} \frac{\partial q}{\partial t} &= \frac{D_s}{\rho^2}\frac{\partial}{\partial \rho}\left(\rho^2 \frac{\partial q}{\partial \rho}\right), \\ \overline{q}(r,t) &= \frac{3}{R_p^3}\int_0^{R_p} \rho^2\, q(r,\rho,t)\, d\rho. \end{aligned} \tag{5}$$

The scales are coupled at the granule surface $(\rho = R_p)$ by flux continuity between the film and the intraparticle diffusion, and by local Langmuir equilibrium,

$$\begin{aligned} \rho_p D_s \left.\frac{\partial q}{\partial \rho}\right|_{\rho=R_p} &= k_f(r)\ (C - C_s)\,, \\ q|_{\rho=R_p} &= \frac{q_{\max} K_L C_s}{1 + K_L C_s}, \end{aligned} \tag{6}$$

with the centre symmetry condition $\partial q/\partial \rho|_{\rho=0} = 0$ and the surface liquid concentration C_s. A dimensional check of (6): the left side is $kg\,m^{-3} \cdot m^2\,s^{-1} \cdot \left(g\,kg^{-1}\right)\ m^{-1} = g\,m^{-2}\,s^{-1}$ and the right side is $m\,s^{-1} \cdot g\,m^{-3} = g\,m^{-2}\,s^{-1}$, i.e. both are surface mass-flux densities.

Initial and boundary conditions. The filter is initially clean, $C(r,0) = 0$, $q(r,\rho,0) = 0$. At the outer inlet a Danckwerts (flux) condition is imposed, and at the inner core a zero-gradient outflow condition,

$$\begin{aligned} \left.\left(u_r C - D_r \frac{\partial C}{\partial r}\right)\right|_{r=R_{out}} &= u_r C_0, \\ \left.\frac{\partial C}{\partial r}\right|_{r=R_{in}} &= 0. \end{aligned} \tag{7}$$

3. Dimensionless formulation and limiting cases

Introduce the normalised radius, concentration, loading, and time

$$\begin{aligned} R &= \frac{r - R_{in}}{R_{out} - R_{in}}, \\ \widehat{C} &= \frac{C}{C_0}, \\ \widehat{q} &= \frac{\overline{q}}{q_0}, \\ \widehat{t} &= \frac{t}{t_c}, \\ t_c &= \frac{\pi L \varepsilon\ \left(R_{out}^2 - R_{in}^2\right)}{Q}, \end{aligned} \tag{8}$$

where t_c is the mean pore-residence (transit) time and $q_0 = q_{\max} K_L C_0/(1 + K_L C_0)$ the loading in equilibrium with C_0. Substituting into (2) gives the dimensionless macro equation

$$\begin{aligned} &\frac{\partial \widehat{C}}{\partial \widehat{t}} + \Lambda \frac{\partial \widehat{q}}{\partial \widehat{t}} \\ &= \frac{1}{Pe_r}\,\frac{1}{\widetilde{r}}\frac{\partial}{\partial R}\left(\widetilde{r}\,\frac{D_r}{D_r^{out}}\frac{\partial \widehat{C}}{\partial R}\right) - \widehat{u}_r(R)\frac{\partial \widehat{C}}{\partial R}, \end{aligned} \tag{9}$$

with $\widetilde{r} = r/(R_{out} - R_{in})$, $\widehat{u}_r = u_r t_c/(R_{out} - R_{in})$, and the two macro groups

$$\begin{aligned} Pe_r &= \frac{|u_r\ (R_{out})|\ (R_{out} - R_{in})}{D_r^{out}}, \\ \Lambda &= \frac{\rho_b q_0}{\varepsilon C_0}\,. \end{aligned} \tag{10}$$

The granule problem (5)–(6) contributes the Biot number and the granule diffusion time,

$$\begin{aligned} Bi(r) &= \frac{k_f(r) R_p C_0}{\rho_p D_s q_0}, \\ \tau_p &= \frac{R_p^2}{D_s}. \end{aligned} \tag{11}$$

With the definition (11), Bi measures the ratio of the intraparticle-diffusion conductance to the film conductance: *large Bi* means the film offers little resistance and intraparticle diffusion controls, whereas *small Bi* means film control. Because $Bi \propto 1/D_s$, a very fast intraparticle diffusion ($D_s \to \infty$) drives $Bi \to 0$, not $Bi \to \infty$; the two limits are distinct and are not to be conflated (this corrects a common misstatement).

Radius-dependent Damköhler number. The local rate competition is measured by

$$\begin{aligned} Da_p(r) &= \frac{\tau_p}{\tau_{res}(r)}, \\ \tau_{res}(r) &= \frac{R_{out} - R_{in}}{|u_r(r)|} \propto r, \end{aligned} \tag{12}$$

the ratio of the intraparticle diffusion time to a local contact time. Since $|u_r| \propto 1/r$, Da_p is smallest at the outer surface and largest near the core. (The cumulative transit time from the outer surface to radius r, obtained rigorously as $t(r) = \int_r^{R_{out}} dr'/|u_r(r')| = \frac{\pi L \varepsilon}{Q}\left(R_{out}^2 - r^2\right)$,

scales as r^2; equation (12) uses the local velocity as a compact per-radius contact-time estimate.) For $Da_p \ll 1$ the granule equilibrates within the contact time, whereas for $Da_p \gg 1$ intraparticle diffusion is rate-limiting.

Reduction to the LDF model. Two independent limits are required to recover the classical LDF law, and they must be distinguished. First, when intraparticle diffusion is fast on the contact-time scale $(Da_p \to 0)$, the loading equilibrates across the granule, $q(\rho) \approx \overline{q}$, and the Glueckauf approximation gives

$$\begin{aligned} \frac{\partial \overline{q}}{\partial t} &\approx k_{LDF}\ \left(q^*\left(C_s\right) - \overline{q}\right), \\ k_{LDF} &= \frac{15 D_s}{R_p^2}, \\ q^*\left(C_s\right) &= \frac{q_{\max} K_L C_s}{1 + K_L C_s}, \end{aligned} \tag{13}$$

which is driven by the *surface* concentration C_s. Second, only when the film resistance is additionally negligible ($Bi \to \infty$, hence $C_s \to C$) does (13) become the textbook LDF law driven by the *bulk* concentration C. Thus the present two-scale model contains the LDF model as the combined fast-diffusion/negligible-film limit, which we use below as a verification benchmark; conversely, when D_s is small (typical for GAC) the resolved model is required.

4. Numerical method

Problem (2)–(7) has variable coefficients and a granule problem attached to every macro point, and is solved numerically. The method rests on three elements: a conservative finite-volume macro discretisation on an equal-volume grid, Strang operator splitting of transport and sorption, and a spectral reduction of the granule problem.

Macro discretisation. The interval $[R_{in}, R_{out}]$ is divided into N cells of equal bulk volume by making the faces uniform in $s = r^2$,

$$r_{i+1/2} = \sqrt{R_{in}^2 + i\,\frac{R_{out}^2 - R_{in}^2}{N}}, \quad i = 0, \ldots, N, \tag{14}$$

so that every cylindrical ring has the same volume $\pi\left(r_{i+1/2}^2 - r_{i-1/2}^2\right) L$ and the advective Courant number is equalised across cells. Equation (2) is integrated conservatively over each ring. The advective solute flux across the face at $r_{i+1/2}$ is $Q\,C_{up}$, evaluated by first-order upwinding (with inward flow the upstream cell is the outer one); the dispersive face flux is $\varepsilon\, 2\pi L\, D_r\left(r_{i+1/2}\right)\, r_{i+1/2}\, \left(C_{i+1} - C_i\right)/(r_{i+1} - r_i)$. Both transport terms are treated *implicitly*, which makes the transport step unconditionally stable and free of the diffusive step restriction $\Delta t \sim \Delta r^2$; the resulting system is tridiagonal and is solved by the Thomas algorithm in $O(N)$ operations. The Danckwerts flux QC_0 enters at the outer face and a zero-gradient advective outflow at the inner face.

Spectral reduction of the granule problem. A direct multi-node discretisation of (5) at every macro cell would be prohibitively expensive; a spectral expansion is used instead, and no separate finite-volume granule grid is employed in the reported computations. With the substitution $u = \rho q$, equation (5) becomes the one-dimensional heat equation $u_t = D_s u_{\rho\rho}$ on $\left[0, R_p\right]$ with $u(0) = 0$ and $u\left(R_p\right) = R_p q_s$, where $q_s = q|_{\rho = R_p}$. Writing $q(\rho, t) = q_s(t) + \sum_{m=1}^{M} a_m(t)\varphi_m(\rho)$ with the eigenfunctions of the homogeneous operator,

$$\begin{aligned} \varphi_m(\rho) &= \frac{1}{\rho}\sin\left(\frac{m\pi\rho}{R_p}\right), \\ \lambda_m &= D_s\left(\frac{m\pi}{R_p}\right)^2, \\ \varphi_m\left(R_p\right) &= 0, \\ \varphi_m|_{\rho \to 0} &\ \text{finite}, \end{aligned} \tag{15}$$

so that q_s acts as a time-dependent lifting term. Projection onto $\{sin\left(m\pi\rho/R_p\right)\}$, orthogonal on $\left[0, R_p\right]$ with $\int_0^{R_p} \sin^2\left(m\pi\rho/R_p\right)\, d\rho = R_p/2$, yields decoupled scalar modal equations $\dot{a}_m + \lambda_m a_m = -\gamma_m \dot{q}_s$; the average (5) follows from $\int_0^{R_p} \rho^2 \varphi_m\, d\rho$. The projection and averaging coefficients are

$$\begin{aligned} \gamma_m &= \frac{2R_p(-1)^{m+1}}{m\pi}, \\ \beta_m &= \frac{3(-1)^{m+1}}{m\pi R_p}, \end{aligned} \tag{16}$$

and a backward-Euler update gives, unconditionally stably,

$$\begin{aligned} a_m^{n+1} &= \frac{a_m^n - \gamma_m\left(q_s^{n+1} - q_s^n\right)}{1 + \lambda_m \Delta t}, \\ \overline{q}^{\,n+1} &= q_s^{n+1} + \sum_{m=1}^{M} \beta_m a_m^{n+1}. \end{aligned} \tag{17}$$

The modal-truncation error decays exponentially in M (demonstrated in Section 5); $M = 6$ modes are used.

Sorption coupling and Newton solve. In the split sorption stage, each cell is updated implicitly. With $q_s^{n+1} = q^*\left(C_s^{n+1}\right)$ the Langmuir surface value, $\overline{q}^{\,n+1}\left(C_s^{n+1}\right)$ from (17), and the local liquid mass balance $C^{n+1} = C^* - \frac{\rho_b}{\varepsilon}\left(\overline{q}^{\,n+1} - \overline{q}^{\,n}\right)$ (where C^* is the post-transport

concentration), the film continuity (6) written as a granule mass balance gives the scalar residual

$$F\left(C_s^{n+1}\right) = \rho_p \frac{\overline{q}^{\,n+1}\left(C_s^{n+1}\right) - \overline{q}^{\,n}}{\Delta t} - \frac{3k_f(r)}{R_p}\left(C^{n+1}\left(C_s^{n+1}\right) - C_s^{n+1}\right) = 0, \tag{18}$$

solved by Newton's method with the analytic derivative F', initial guess C_s^n, tolerance $|\Delta C_s| \leqslant 10^{-11}\,(1 + |C_s|)$, at most 40 iterations, and the projection $C_s \leftarrow \max(C_s, 0)$ enforcing non-negativity; the only nonlinearity is the scalar Langmuir isotherm. Because the granule problems in different cells are independent, this stage vectorises across cells.

Time stepping. Strang splitting is used: a half transport step, a full sorption step, and a half transport step, giving second-order accuracy in time; the ordering (transport–sorption–transport) is fixed throughout, and all reported figures use this scheme. As both sub-steps are unconditionally stable, the step is limited by accuracy rather than stability; a fixed step is used and its adequacy is established by the time-step convergence study in Section 5. First-order Lie splitting is available as an option and was used only to confirm the temporal order.

5. Results and discussion

A representative computation was carried out for a granular-activated-carbon cartridge treating a dilute organic micropollutant. The physical parameters (Table 1) are representative literature values for GAC adsorption of organic micropollutants [2, 7, 10]: a surface diffusivity $D_s = 2 \times 10^{-12}\,m^2\,s^{-1}$, granule radius $R_p = 0.5\,mm$, and a Langmuir capacity $q_{\max} = 120\,g\,kg^{-1}$ are typical of this class of systems. The film and dispersion coefficients are computed from (3)–(4) with $D_m = 10^{-9}\,m^2\,s^{-1}$, $\nu = 10^{-6}\,m^2\,s^{-1}$, and $\alpha_L = 1\,mm$; the calculation is presented as a representative illustrative case rather than a fitted prediction for a specific field system.

Table 1. Parameters of the representative computation (representative GAC/organic-micropollutant values).

Parameter	Symbol	Value	Unit
Core radius	R_{in}	5.0×10^{-3}	m
Outer radius	R_{out}	2.5×10^{-2}	m
Cartridge height	L	0.10	m
Porosity	ε	0.40	–
Granule density	ρ_p	700	$kg\,m^{-3}$
Granule radius	R_p	5.0×10^{-4}	m
Surface diffusion coeff.	D_s	2.0×10^{-12}	$m^2\,s^{-1}$
Molecular diffusivity	D_m	1.0×10^{-9}	$m^2\,s^{-1}$
Kinematic viscosity	ν	1.0×10^{-6}	$m^2\,s^{-1}$
Longitudinal dispersivity	α_L	1.0×10^{-3}	m
Volumetric flow rate	Q	5.0×10^{-7}	$m^3\,s^{-1}$
Inlet concentration	C_0	50	$g\,m^{-3}$
Saturation loading	$q_{\max}$	120	$g\,kg^{-1}$
Langmuir constant	K_L	0.05	$m^3\,g^{-1}$
Radial cells	N_r	100	–
Granule modes	M	6	–
Simulation time	t_{end}	6.0×10^5 ($\approx 167\,h$)	s

For these parameters the dimensionless groups are $Pe_r \approx 19.8$, $\Lambda \approx 1.8 \times 10^3$, $\tau_p \approx 1.25 \times 10^5\,s$, with a radius-dependent film Biot number $Bi \approx 0.9$ at the outer surface and ≈ 1.7 near the core (film coefficient $k_f \approx 4.4 \times 10^{-6}$ to $8.1 \times 10^{-6}\,m\,s^{-1}$). The interstitial velocity increases from $|u_r\,(R_{out})| \approx 8.0 \times 10^{-5}\,m\,s^{-1}$ to $|u_r\,(R_{in})| \approx 4.0 \times 10^{-4}\,m\,s^{-1}$, i.e. a five-fold velocity ratio across the bed. The corresponding radius-dependent Damköhler number is $Da_p \approx 5.0 \times 10^2$ at the outer surface and $\approx 2.5 \times 10^3$ near the core. These values, recomputed consistently from Table 1, differ by several orders of magnitude from the erroneous value $Da \approx 3 \times 10^{-2}$ that appeared in an earlier draft; the correct interpretation is that the process is *intraparticle-diffusion limited throughout* ($Da_p \gg 1$), more severely near the core, rather than kinetically fast.

Radial and space–time behaviour. Figure 1 shows the radial profiles of the liquid concentration C/C_0 and of the granule-averaged loading $\overline{q}/q_{\max}$ at several times. Adsorption starts at the outer inlet and the loading front advances inward; the averaged loading (not the intra-granule field) is plotted. Figure 2 shows the space–time concentration field and its 5%, 50%, and 95% contours; the 50% contour is the midpoint of the adsorption front, and the 5%–95% separation measures the mass-transfer-zone width. Figures 3–4 give the three-dimensional surface and the annular cross-sections, which display the inward-moving front directly.

Breakthrough and the role of the radial velocity. Figure 5 shows the outlet breakthrough curve $C\,(R_{in}, t)\,/C_0$, together with a controlled comparison against a uniform-velocity bed of identical geometry, capacity, and mean residence time. The breakthrough metrics are given in Table 2. The central, and deliberately conservative, finding is that at constant intraparticle diffusivity the radial $(1/r)$ velocity field has only a modest influence on the outlet response: because the rate is limited by the (radius-independent) intraparticle diffusion, the two breakthrough curves nearly coincide, and the ultimate capacity utilisation is essentially identical. The radial velocity, acting through the velocity-dependent film coefficient, shifts the early breakthrough time by roughly one quarter and redistributes the internal loading, but it does not qualitatively change the outlet behaviour. In particular, the earlier saturation of the outer layers is largely the generic inlet-first saturation of any fixed bed and is present under uniform velocity as well; it is not, by itself, a signature of the $1/r$ field. This clarifies and corrects the stronger claim made in an earlier draft.

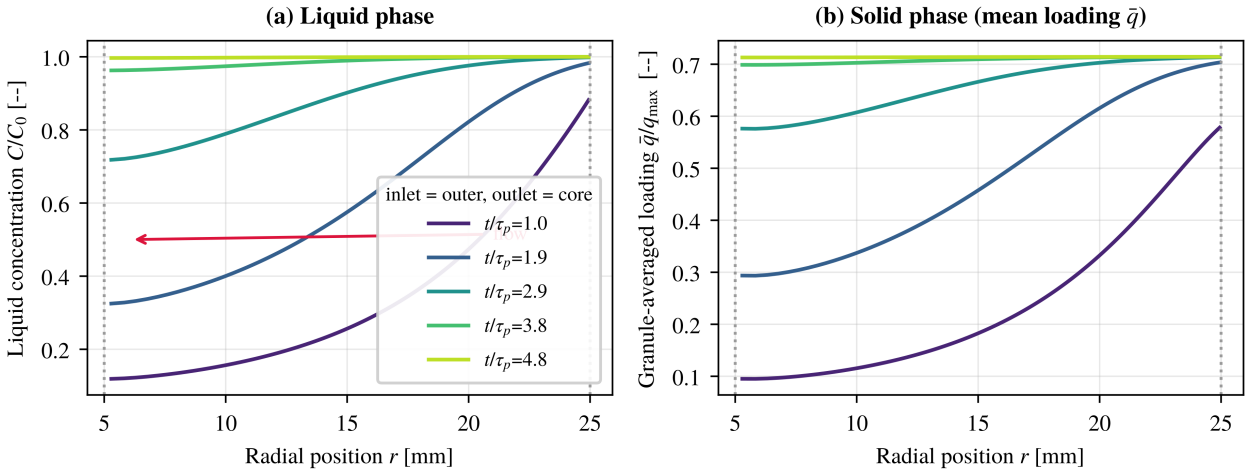


Figure 1. Radial profiles at $t/\tau_p = 1.0, 1.9, 2.9, 3.8, 4.8$: (a) liquid concentration C/C_0; (b) granule-averaged loading $\overline{q}/q_{\max}$. Flow is inward, from the outer inlet ($r = R_{out} = 25\,mm$) to the core outlet ($r = R_{in} = 5\,mm$).

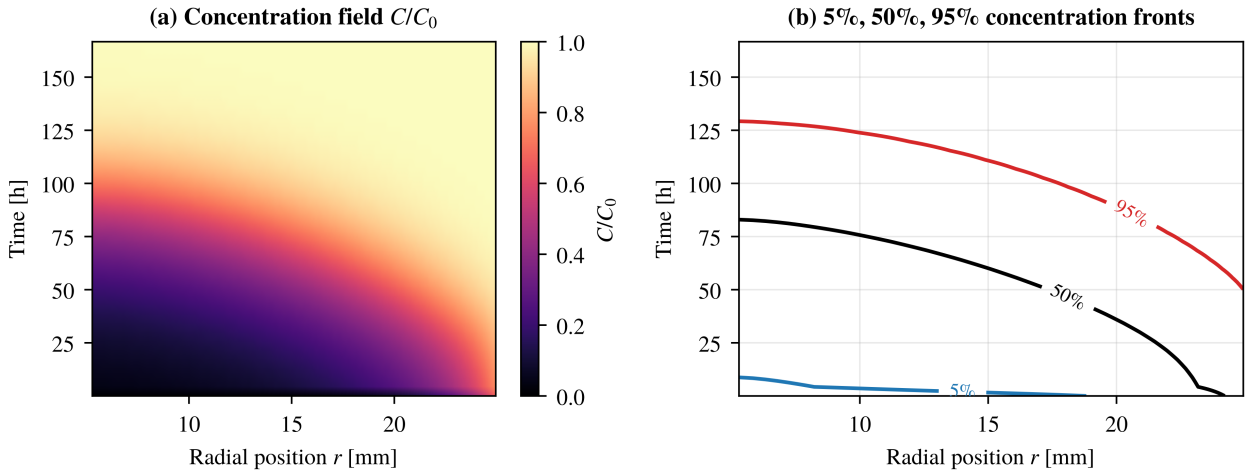


Figure 2. Space–time evolution of C/C_0: (a) field map; (b) 5%, 50%, and 95% concentration fronts. The front reaches the core (outlet) later than the outer surface (inlet).

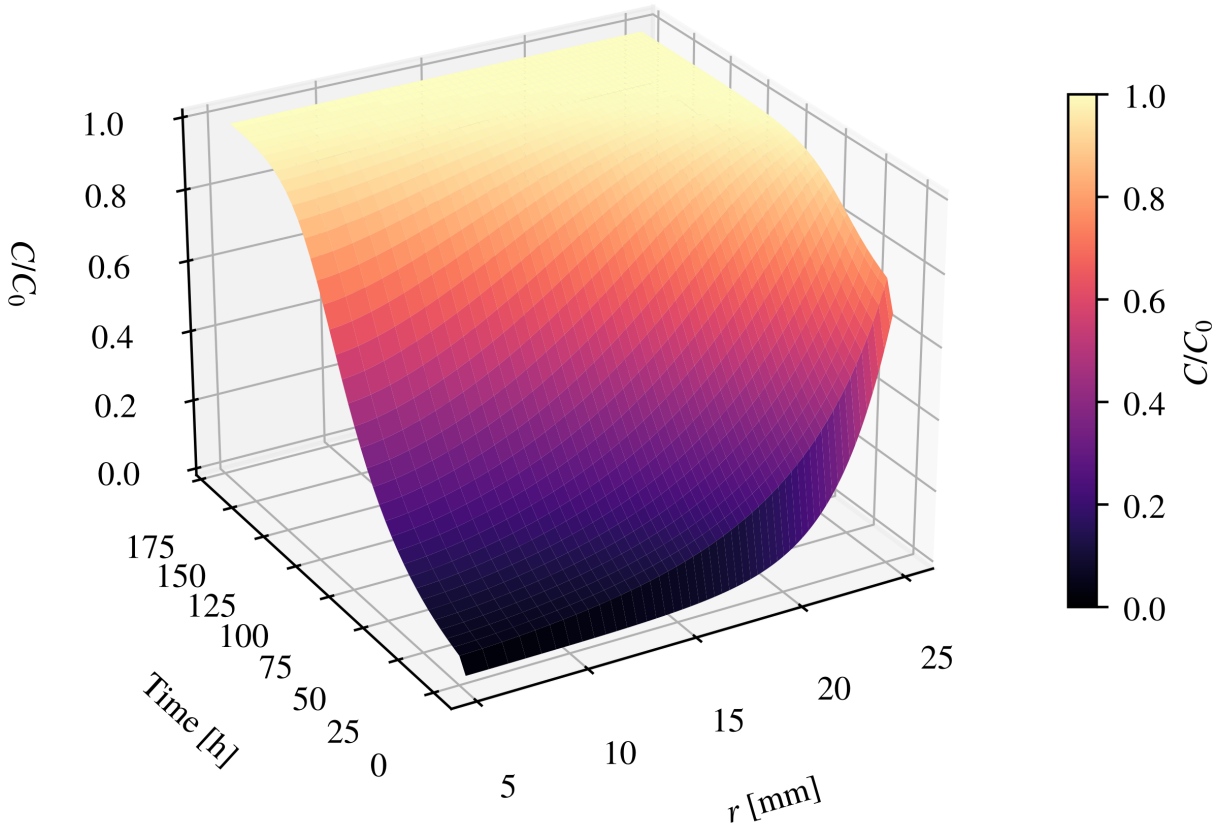


Figure 3. Three-dimensional view of the concentration field $C(r,t)/C_0$.

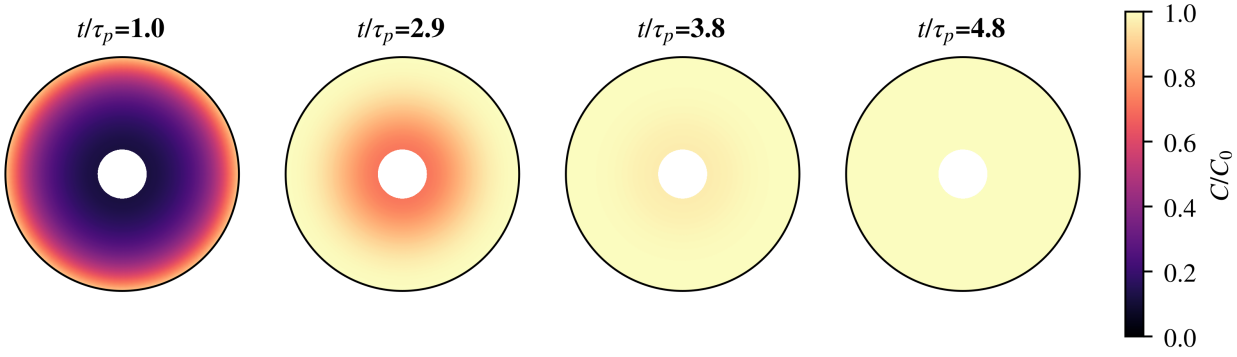


Figure 4. Annular cross-section (top view) of C/C_0 at $t/\tau_p = 1.0, 2.9, 3.8, 4.8$; the central hole is the perforated core (outlet). The saturation front propagates radially inward.

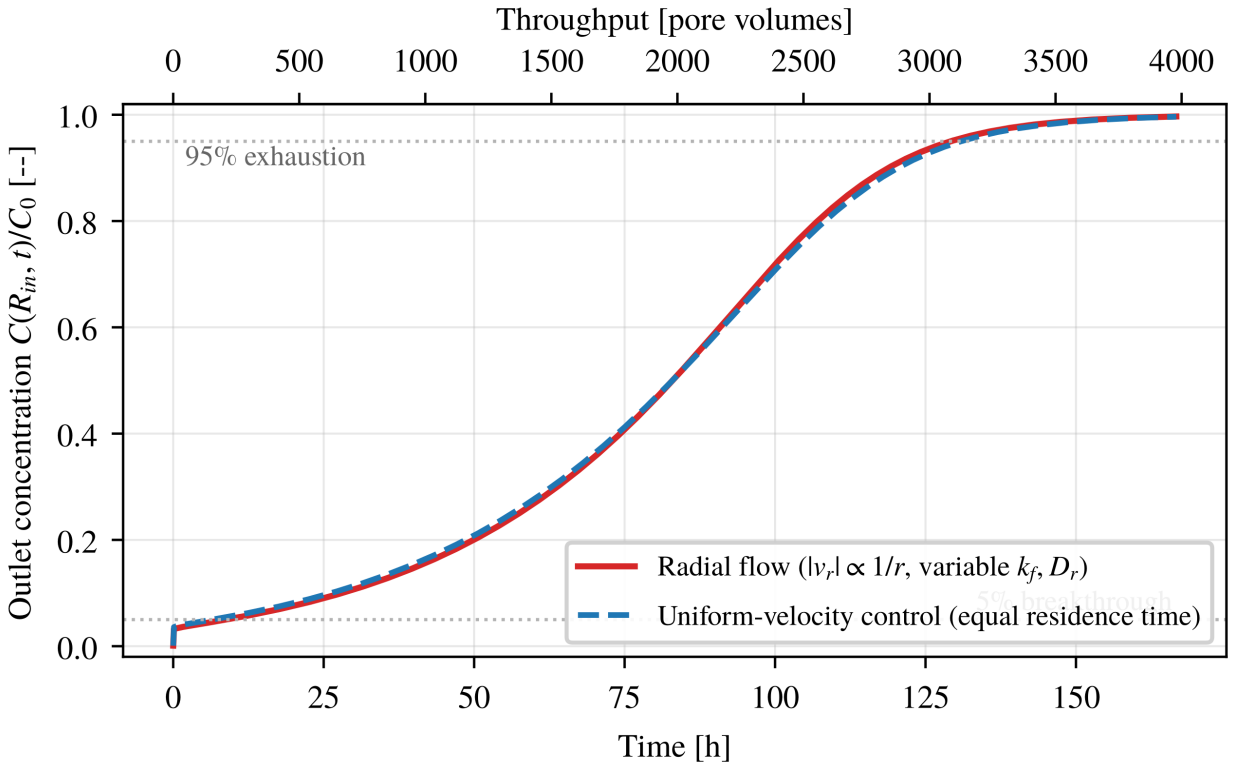


Figure 5. Breakthrough curve at the core outlet for the radial-flow filter (variable k_f, D_r) and for a uniform-velocity control bed of equal residence time. Top axis: throughput in pore volumes.

Table 2. Breakthrough metrics (5% breakthrough and 95% exhaustion criteria).

Quantity	Radial flow	Uniform-velocity control
Breakthrough time t_b ($C/C_0 = 0.05$)	≈ 8.8 h	≈ 6.5 h
Exhaustion time t_e ($C/C_0 = 0.95$)	≈ 129 h	≈ 131 h
Breakthrough volume $V_b = Qt_b$	$1.6 \times 10^{-2}\, m^3$	$1.2 \times 10^{-2}\, m^3$
Saturation volume $V_e = Qt_e$	$2.3 \times 10^{-1}\, m^3$	$2.4 \times 10^{-1}\, m^3$
Capacity utilisation at t_{end}	0.999	0.999

Parameter sensitivity. A one-at-a-time sensitivity study (each parameter halved and doubled) confirms the diffusion-limited picture. The capacity utilisation at t_{end} is most sensitive to the flow rate Q (from 0.90 at $Q/2$ to 1.00 at $2Q$) and to the granule radius R_p (from 1.00 at $R_p/2$ to 0.95 at $2R_p$, since $\tau_p \propto R_p^2$), and is only weakly sensitive to D_s, k_f, and D_r over the range explored, because intraparticle diffusion and total residence time jointly control the outcome.

Numerical verification. Verification is reported within this paper rather than deferred. (i) *Grid convergence:* refining the radial grid $N_r = 50, 100, 200, 400$ changes the breakthrough curve negligibly (Fig. 6a); the adsorbed mass at t_{end} varies by $< 0.1\%$ between $N_r = 100$ and 400. (ii) *Time-step convergence:* halving Δt down to 12.5 s changes the adsorbed mass monotonically and by $< 0.3\%$ over the last refinement, confirming that the production step is adequate. (iii) *Modal convergence:* the relative error in the adsorbed mass decays exponentially in M (Fig. 6b), so $M = 6$ modes are more than sufficient. (iv) *Global mass conservation:* the normalised balance residual $\left(M_{in} - M_{liquid} - M_{adsorbed} - M_{out}\right)/M_{in}$ remains at machine precision ($\sim 10^{-13}$) throughout, as expected for the conservative finite-volume scheme. (v) *Positivity and boundedness:* the computed fields satisfy $0 \leqslant C \leqslant C_0$ and $0 \leqslant \overline{q} \leqslant q_{\max}$ at all times, with no clipping required beyond the non-negativity projection in the Newton solve. (vi) *Limiting-case validation:* in the fast-diffusion, negligible-film regime the two-scale solution reproduces the analytical LDF result (13), confirming the internal consistency of the coupling.

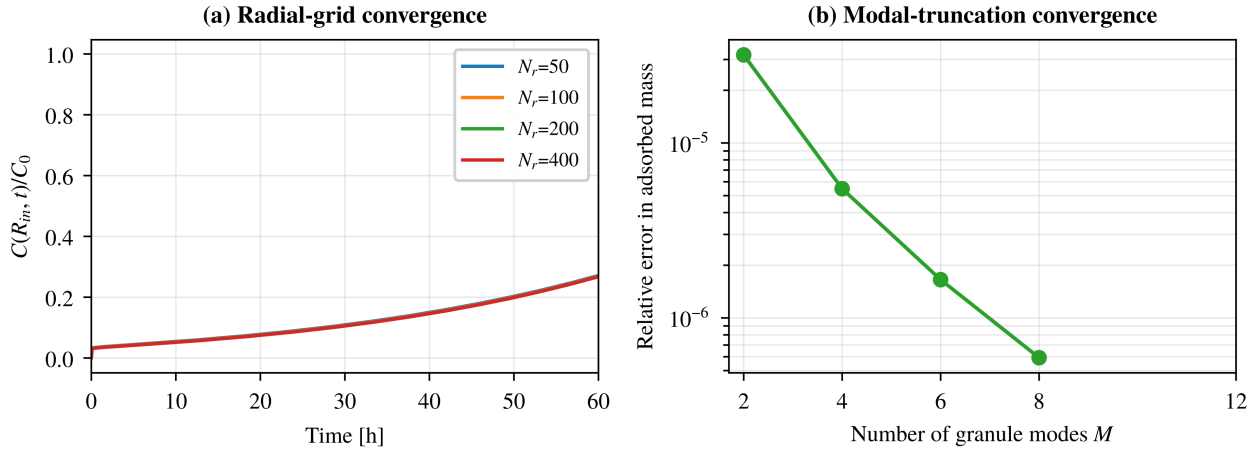


Figure 6. Numerical verification: (a) radial-grid convergence of the breakthrough curve ($N_r = 50, 100, 200, 400$, curves overlapping); (b) exponential decay of the modal-truncation error in the adsorbed mass with the number of granule modes M.

Scope and limitations. The model is a radial one-dimensional macro model: axial variations from inlet distribution, end effects, core perforation, and packing nonuniformity are neglected, and the approximation is appropriate for long cartridges with well-distributed inlet flow. The flow field is a prescribed incompressible radial field, not a Darcy-pressure solution; if a pressure field were required (e.g. for compressible or clogging beds) a permeability relation would have to be added. Multicomponent competition, temperature effects, and a velocity-dependent surface diffusivity are outside the present scope.

6. Conclusions

A two-scale model and a verified numerical method have been developed for mass transport and adsorption in a cylindrical radial-flow filter. The macroscopic advection–dispersion equation, written consistently in terms of the interstitial velocity $|u_r| \propto 1/r$ and closed with velocity-dependent film and dispersion coefficients, is coupled to resolved intraparticle surface diffusion through film transfer and local Langmuir equilibrium. The complete dimensionless problem has been derived; the governing groups have been recomputed consistently, giving an intraparticle-diffusion-limited regime with a radius-dependent Damköhler number $Da_p \sim 10^2$–10^3, and the model has been shown to reduce to the classical LDF law in the combined fast-diffusion, negligible-film limit. The conservative finite-volume/spectral-reduction algorithm has been verified within the paper through grid, time-step, and modal convergence, machine-precision mass conservation, solution positivity, and agreement with the LDF limit. A controlled comparison with a uniform-velocity bed shows that, at constant intraparticle diffusivity, the radial velocity field mainly redistributes the internal loading and shifts the early breakthrough modestly, while leaving the outlet breakthrough and the ultimate utilisation close to the uniform-velocity case. The framework provides a sound and reproducible basis for predicting breakthrough and service capacity of radial-flow cartridges and for future extensions to multicomponent systems and velocity-dependent intraparticle transport.

Declarations

Author Contributions: Conceptualization, B.I.B., methodology, B.I.B., software, B.I.B. and L.S.U., validation, M.U.E., visualization, M.U.E., writing—original draft preparation, B.I.B., writing—review and editing, M.U.E. and L.S.U. All authors have read and agreed to the published version of the manuscript.

Funding: This research received no specific grant from any funding agency in the public, commercial, or not-for-profit sectors.

Ethics Approval: Not applicable. This mathematical and numerical study did not involve human participants or animal subjects.

Informed Consent and Consent for Publication: Not applicable. This study does not report human participants or identifiable personal data.

Data Availability Statement: The numerical code (finite-volume/spectral-reduction solver) and the data underlying all figures and tables, including the convergence-test and breakthrough data, are available from the corresponding author on reasonable request.

Acknowledgments: No acknowledgments are specified in the submitted manuscript. The authors should confirm whether additional acknowledgments are appropriate before publication.

Conflicts of Interest: The authors declare no conflict of interest.

Artificial Intelligence Disclosure: An AI assistant was used for technical LaTeX typesetting of this manuscript. The authors should verify and approve the statement and disclose any additional reportable AI use, if applicable; this statement does not establish AI use in the underlying scientific work.

Nomenclature and Abbreviations

Symbol / acronym	Definition
C	liquid concentration ($g\ m^{-3}$)
D_m	molecular diffusivity
C_s	surface liquid concentration
k_f	film coefficient
C_0	inlet concentration
α_L	dispersivity
q	intra-granule loading ($g\ kg^{-1}$)
ν	kinematic viscosity
$\overline{q}$	granule-averaged loading
ε	porosity
q_0	loading in equilibrium with C_0
ρ_p, ρ_b	granule and bulk density
r, ρ	macro and granule radial coordinates (m)
$q_{\max}, K_L$	Langmuir parameters
R_{in}, R_{out}, R_p	core, outer, granule radii
Pe_r	radial Peclet
L	height
Λ	capacity ratio
Q	volumetric flow rate ($m^3\ s^{-1}$)
Bi	Biot number
q_r, u_r	superficial and interstitial velocities ($m\ s^{-1}$)
τ_p	granule diffusion time
D_r	radial dispersion
Da_p	radius-dependent Damköhler number
D_s	surface diffusivity
Sh, Re_p, Sc	Sherwood, particle Reynolds, Schmidt numbers
GAC	Granular activated carbon
LDF	Linear-driving-force adsorption approximation
HSDM	Homogeneous surface diffusion model

References

[1] Qasem NAA, Mohammed RH, Lawal DU. Removal of heavy metal ions from wastewater: a comprehensive and critical review. npj Clean Water. 2021;4:36. https://doi.org/10.1038/s41545-021-00127-0.

[2] Ruthven DM. Principles of Adsorption and Adsorption Processes. John Wiley & Sons; 1984.

[3] Langmuir I. The adsorption of gases on plane surfaces of glass, mica and platinum. J Am Chem Soc. 1918;40(9):1361–1403. https://doi.org/10.1021/ja02242a004.

[4] Dima JB, Ferrari MA, Zaritzky N. Mathematical modeling of breakthrough curves in dynamic column adsorption: analytical solutions and validation. J Eng Math. 2024;147:5. https://doi.org/10.1007/s10665-024-10375-x.

[5] Patel H. Fixed-bed column adsorption study: a comprehensive review. Appl Water Sci. 2019;9:45. https://doi.org/10.1007/s13201-019-0927-7.

[6] Xu Z, Cai JG, Pan BC. Mathematically modeling fixed-bed adsorption in aqueous systems. J Zhejiang Univ Sci A. 2013;14(3):155–176. https://doi.org/10.1631/jzus.A1300029.

[7] Zhang Q, Crittenden J, Hristovski K, et al. User-oriented batch reactor solutions to the homogeneous surface diffusion model for different adsorption kinetics. Chem Eng Sci. 2009;64(13):3010–3019. https://doi.org/10.1016/j.ces.2009.03.031.

[8] Sperlich A, Schäfer D, Worch E, et al. Breakthrough behavior of granular ferric hydroxide fixed-bed adsorption filters. J Water Supply Res Technol AQUA. 2005;54(3):155–164.

[9] León G, García F, Pérez A, et al. Homogeneous diffusion solid model as a realistic approach to describe adsorption onto materials with different geometries. Molecules. 2021;26(17):5314. https://doi.org/10.3390/molecules26175314.

[10] Zhang W, Dong L, Yan H, et al. Diffusion of hydrophilic organic micropollutants in granular activated carbon with different pore sizes. Water Res. 2019;158:211–222. https://doi.org/10.1016/j.watres.2019.04.020.

[11] Glueckauf E. Theory of chromatography. Part 10. Formulæ for diffusion into spheres and their application to chromatography. Trans Faraday Soc. 1955;51:1540–1551. https://doi.org/10.1039/TF9555101540.

[12] Crank J. The Mathematics of Diffusion. 2nd ed. Clarendon Press; 1975.

[13] Bird RB, Stewart WE, Lightfoot EN. Transport Phenomena. 2nd ed. John Wiley & Sons; 2002.

[14] Bear J. Dynamics of Fluids in Porous Media. American Elsevier; 1972.

[15] Wakao N, Funazkri T. Effect of fluid dispersion coefficients on particle-to-fluid mass transfer coefficients in packed beds. Chem Eng Sci. 1978;33(10):1375–1384. https://doi.org/10.1016/0009-2509(78)85120-3.

[16] Pérez Guerrero JS, Skaggs TH. Analytical solution for one-dimensional advection–dispersion transport equation with distance-dependent coefficients. J Hydrol. 2010;390(1–2):57–65. https://doi.org/10.1016/j.jhydrol.2010.06.030.

[17] Han F, Huang Y, Hao C, et al. A novel radial flow adsorber with uniform velocity distribution for air purification in liquid air energy storage. Renew Energy. 2025;240:122197. https://doi.org/10.1016/j.renene.2024.122197.

[18] Zhang Y, Ba L, Fan W, et al. Two-dimensional modeling of pressure swing adsorption (PSA) oxygen generation with radial-flow adsorber. Appl Sci. 2019;9(6):1153. https://doi.org/10.3390/app9061153.

[19] Hosseini SS, Sari A, Rahimi A. A modeling analysis on industrial radial-flow packed-bed reactors for the catalytic dehydrogenation of long-chain normal paraffins. Chem Eng Res Des. 2024;212:121–133. https://doi.org/10.1016/j.cherd.2024.10.030.
[20] Ravshanov N, Boborahimov BI, Berdiyorov ShSh. Numerical modeling of filtration and transport processes in a cylindrical porous filter using the finite volume method. Probl Comput Appl Math. 2026;1(71):28–42.
[21] Raoof A, Hassanizadeh SM. Upscaling transport of adsorbing solutes in porous media: pore-network modeling. Vadose Zone J. 2010;9(3):624–636. https://doi.org/10.2136/vzj2010.0026.

Disclaimer of Liability/Publisher's Note

The statements, opinions, and data contained in all publications are solely those of the individual author(s) and contributor(s) and do not necessarily reflect the views of the Publisher, the Journal, or the editors. The Publisher, the Journal, and the editors disclaim responsibility for any injury to persons or damage to property resulting from any ideas, methods, instructions, or products referred to in the content.